Tailored resonance in micrometer-sized monoaxial chiral helimagnets

F. J. T. Goncalves,[1,2,*] T. Sogo,[1] Y. Shimamoto,[1] I. Proskurin,[3,4,2] Vl. E. Sinitsyn,[4] Y. Kousaka,[2,5] I. G. Bostrem,[4] J. Kishine,[6,2] A. S. Ovchinnikov,[4,7] and Y. Togawa[1,2]

[1]*Department of Physics and Electronics, Osaka Prefecture University, 1-1 Gakuencho, Sakai, Osaka 599-8531, Japan*
[2]*Chirality Research Centre, Hiroshima University, Higashi-Hiroshima, Hiroshima 739-8526, Japan*
[3]*Department of Physics and Astronomy, University of Manitoba, Winnipeg, Manitoba R3T 2N2, Canada*
[4]*Institute of Natural Sciences, Ural Federal University, Ekaterinburg 620083, Russia*
[5]*Graduate School of Science, Okayama University, Okayama 700-8530, Japan*
[6]*Division of Natural and Environmental Sciences, The Open University of Japan, Chiba 261-8586, Japan*
[7]*Institute for Metal Physics, Ural Division of RAS, Ekaterinburg 620137, Russia*

(Received 25 April 2018; revised manuscript received 24 August 2018; published 8 October 2018)

We discuss how the collective magnetic resonance response of the monoaxial chiral helimagnetic crystal $CrNb_3S_6$ can be tailored by changing the area of its magnetization plane. Micrometer-sized samples of this crystal yield a number of resonance modes occurring at frequencies ranging from 15 to 20 GHz, even in the absence of a magnetic field. Changes in the resonance bandwidth, of the order of several GHz, are attributed to the effect of the spatially nonuniform demagnetization fields on standing spin wave modes. This material hosts a chiral spin soliton lattice phase, whose field robustness, degree of controllability, and the relatively unexplored polarization-dependent microwave absorption make way for novel microwave applications.

DOI: 10.1103/PhysRevB.98.144407

I. INTRODUCTION

The ability to encode chirality in the propagation of electromagnetic waves in magnetic media is one of the main reasons for the ever-increasing interest in chiral noncollinear spin systems and their potential application in spin electronics, data processing, and storage [1–8].

The formation of noncollinear spin systems with chirality, such as chiral helimagnetic structures, is enabled by the competition between the symmetric and antisymmetric exchange interaction terms [9–12]. The stability of these spin systems can be mediated by anisotropy fields of various origins (crystal, shape, interface pinning) as well as external magnetic fields. The balance between all these contributions gives the ability to finely tune the critical transitions in the magnetization, the resistance, and the microwave absorption properties [13–18].

Among all known chiral helimagnets [3,19], prototype systems capable of stabilizing the chiral helimagnetic phase over a wide range of magnetic field values are of much interest. Here, the particular case of $CrNb_3S_6$ is discussed. Due to a large magnetocrystalline anisotropy, the magnetic moment is bound to an easy plane (ab plane) perpendicular to the chiral (c) axis. The ground state of this chiral helimagnet consists of arrayed 2π magnetic kinks (MKs) winding along the c axis with a period of 48 nm, forming the chiral helimagnetic phase [12–14,19]. In the presence of a magnetic field, H, applied perpendicular to the c axis, the helical phase transforms into a chiral spin soliton lattice (CSL), comprising MKs spaced by regions with field polarized spins. While a relatively small value of H will cause little effect on the periodicity of the CSL, an increasingly large H, approaching a critical value H_C, will promote a more rapid change in the number of MKs. Regardless of the sample geometry and magnetic field strength, the MKs are capable of maintaining their spin structure, changing only their periodicity. Above H_C, the number of MKs is reduced to zero and the forced ferromagnetic (FFM) phase is reached. The relatively simple crystal symmetry, the field robustness, and the long range spatial coherence of the CSL make the crystal $CrNb_3S_6$ an interesting subject for understanding the physics behind chiral helimagnetic structures.

In specimens with dimensions within the micrometer length scale, hysteresis becomes prominent and quatized changes in the CSL density manifest by a stepwise variation of the magnetic moment and magnetoresistance states [14,15,20,21]. Finite geometries as such pose interesting new challenges due to the effects of frustrated local spins and nonuniform demagnetization fields emerging as a consequence of magnetic pole distribution near interfaces of the specimen. A powerful and direct way to probe these effects is via the collective resonance response of both the CSL and the FFM phases. In this front, previous theoretical work showed that the resonant dynamics of the CSL in weakly bounded systems had to be relatively independent of the magnitude of H (at low values of H), and decreased asymptotically in frequency as H approached H_C [22,23], in a behavior similar to the sine-Gordon model for the CSL density [3]. This overall behavior was confirmed experimentally in Ref. [16]. However, it was also observed that the collective resonant response of the CSL was very sensitive to the polarization of the excitation microwave fields. When (I) the in-plane microwave field h_{IP} was set parallel to the c axis, the field dependence of the

*f-goncalves@pe.osakafu-u.ac.jp

obtained resonance mode was generally independent of H at low fields and followed by the asymptotic decrease near H_C. On the other hand, when (II) h_{IP} was set perpendicular to the c axis, the resonance increased linearly in frequency over the whole CSL phase, showing the asymptotic decrease only in the vicinity of H_C. Moreover, uncharacteristic modes were observed in the vicinity of the critical field transitions of the CSL. To clarify the origin of this behavior, further experimental examination of the size dependence and the effect of the microwave field polarization is necessary.

In the present paper, the effect of varying the size of the ab plane is investigated via magnetic resonance experiments. To that end, three specimens with different lengths along the in-plane field direction (perpendicular to the c axis) were examined. In brief, we find that the resonance frequency can vary by several gigahertz with choice of specimen size. Moreover, we show that the resonance modes with uncharacteristic field dependence near the critical field are a consequence of the finite size of the specimens.

The FFM phase of all specimens exhibited three magnetostatic spin wave modes, and their frequency separation increased with decreasing area of the ab plane, suggesting that the overall resonance response depends on the nonuniform demagnetization fields. A model considering the dispersion relation of dipole dominated spin waves in micrometer-sized elements reproduced the multiple resonance modes obtained.

The CSL phase of the sample with the largest magnetization (ab) plane exhibited one resonance mode. A model for the standing spin wave modes in the CSL with finite length and pinned boundaries is consistent with the observation of a single resonance mode. Interestingly, the samples with smaller ab planes exhibited two resonance modes, whose frequency separation increased with decreasing size of the specimen. As a possible scenario, we consider this to be linked to the changes in the spatial profile of the demagnetization fields.

II. EXPERIMENTAL RESULTS

Bulk-size $CrNb_3S_6$ crystals were produced using a chemical vapor transport method [24,25]. Three micrometer-sized samples were cut from the bulk crystal using a focused ion beam technique and welded onto the signal line of coplanar waveguides (CPWs) using tungsten. Figures 1(a)–1(c) shows scanning electron microscopy (SEM) images of the specimens labeled from S1 to S3. Broadband frequency, CPW-type, resonance spectroscopy was employed to probe the collective resonance response of the micrometer-sized crystals. A microwave current (i_{MW}), supplied and analyzed by a vector network analyzer via the forward transmission parameter S_{21}, induces transverse in-plane (h_{IP}) and out-of-plane (h_{OP}) microwave field components which will drive the precession in the specimen. The direction of the c axis, the excitation field components, and H were maintained on all specimens. The orientation of the crystal relative to the static field resembles the configuration (I) examined in Ref. [16], where the resonance signals attributed to the FFM phase and the CSL phase were observed within a magnetic field magnitude of 0.2 T. The quantity S_{21} was acquired as a function of frequency (1 to 40 GHz) and magnetic field, from 0.2 to −0.2 T. A reference spectra was used to subtract the background signal

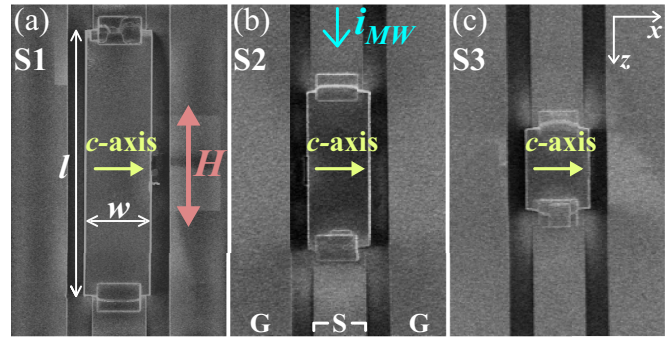

FIG. 1. SEM images of the specimens placed on top of the signal line of a CPW, whose width, $S = 10$ μm, is the same on all specimens. The arrows illustrate the direction of the c axis, H, and the excitation microwave current (i_{MW}). The length, width and thickness (l, w, t) in μm are (49.6, 12.3, 2.4), (30.1, 12.1, 2.6), and (14.7, 12.0, 2.3) for S1, S2, and S3, respectively.

in order to minimize the effect of nonmagnetic features unrelated to the resonance signal of the specimens. The corrected transmission spectra are referred to as ΔS_{21}. All measurements were performed well bellow the Curie temperature of $CrNb_3S_6$ (127 K), at 50 K.

Figures 2(a) 2(c) show the amplitude maps of ΔS_{21} plotted as a function of the frequency of the excitation field, f, and the static magnetic field, H, for the samples S1, S2, and S3, respectively. Following the mode description given below, the data were fitted with the number of Lorentzian line shapes deemed suitable for each specimen and magnetic phase. This allowed an accurate assessment of the peak position, linewidth, and amplitude of each resonance mode as a function of H. Examples of the fitted Lorentzian line shapes are plotted as the continuous lines in Figs. 2(d) 2(i). In some field regions the quality of the fitting decreased due to either the low amplitude of the modes, the close proximity between the resonance modes, or the background noise. Nevertheless, the fitting errors remained lower than the bandwidth of each mode, so the method employed was effective. On all specimens, the field sweep from 0.2 −0.2 T showed the transition from the FFM to the CSL phase at a field $\mu_0 H_J \sim$ 0.1 T and a transition from the CSL to the FFM phase at $\mu_0 H_C \sim -0.145$ T. The phase transitions observed here are consistent with those observed using Lorentz transmission electron microscopy and magnetoresistance measurements on specimens with similar dimensions [14,21,26].

The FFM phase of all samples exhibited three resonance modes whose field dependence is indicated by the field-dependent dashed lines. These resonance lines are all parallel to one another and follow a linear, Kittel-like decrease with decreasing H. Examples of the absorption spectra at 0.16 and −0.16 T can be found in Figs. 2(d), 2(f), and 2(h) for S1, S2, and S3, respectively. Each resonance peak is indicated by a colored arrow. The transition from FFM to the CSL is characterized by a sudden increase in the resonance frequency and a reduction in the number of modes, near H_J.

The resonance in the CSL phase depends weakly on the magnitude of H, except in the field regions near H_J and H_C, where the resonance frequency varies more pronouncedly,

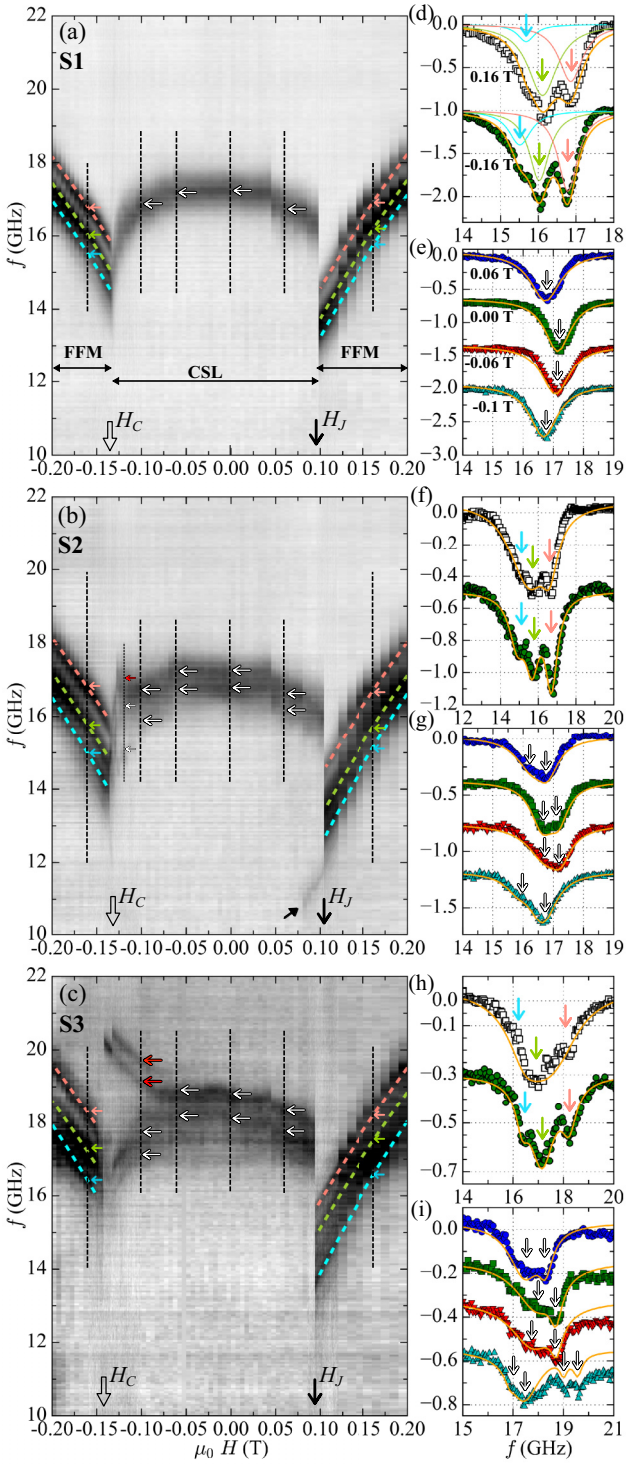

FIG. 2. (a)–(c) Amplitude maps of ΔS_{21} as a function of f and H for S1, S2, and S3, respectively, measured at 50 K, while varying $\mu_0 H$ from 0.2 T to −0.2 T. The tilted arrow in (b) highlights the Kittel-like mode coexisting with the CSL phase. (d)–(i) ΔS_{21} plotted as a function of f in the FFM and CSL phases of each specimen, at the H values shown in (d) and (e). The continuous lines correspond to the Lorentzian fit and the arrows indicate the frequency position of each resonance mode. The three Lorentzian functions shown in (d) illustrate the spectral weight of each mode individually. The vertical dashed lines (arrows) in (a)–(c) indicate the field position of the spectra shown in (d)–(i).

which is consistent with previous experiments [Ref. [16], configuration (I)]. The present study revealed that the absolute value of the resonance frequency and the number of modes changes considerably with varying dimensions of the magnetization plane.

In S1, the CSL phase exhibited one dominant resonance mode with a large absorption amplitude which followed a domelike field dependence with regards to 0 T, with an asymptotic decrease of the resonance frequency near H_C. The CSL phase of $S2$ exhibited two dominant resonances, which appear separated in frequency by 0.5 GHz. Both modes follow a field dependence similar to that of the mode observed in S1. However, in S2 an additional mode with low amplitude, indicated by the red horizontal arrow in Fig. 2(b), appears to extend from the dominant resonance modes near −0.12 T. The resonance frequency of this extended mode follows a linear field dependence until H_C, at which point it vanishes abruptly.

The CSL phase of S3 also exhibited two dominant resonance modes, which have the same field dependence observed in S1 and S2, except that here the frequency splitting between the modes has increased to 0.9 GHz. Interestingly, with increasing the strength of $\mu_0 H$ from −0.07 T to H_C, two additional modes appear at higher frequencies [two red arrows in Fig. 2(c)]. In contrast with the asymptotic decrease in frequency of the dominant modes, the frequency of these two additional modes increases linearly as H approaches H_C.

Figures 3(a)–3(c) show examples of the resonance frequency in the FFM (±0.16 T) and helimagnetic (0 T) states, plotted as a function of the ab-plane area of the three specimens. The main feature observed across all experimental data, in both the FFM and CSL phases, is the increase in the absolute value of the resonance frequency and the mode splitting δf (the frequency separation between modes) as a result of decreasing the size of the specimen along the direction of the applied field. From S1 to S2, the high frequency mode remains unchanged, while the lower frequency mode shifts downwards in frequency by 0.5 GHz. From S2 to S3, there is an overall increase in the resonance frequency of the FFM phase by approximately 1.5 GHz while the frequency splitting increases by 0.15 GHz. In the CSL phase of S1 only one resonance mode is resolved, while in S2 we observed two resonance modes separated in frequency by 0.5 GHz. From S2 to S3, the resonance frequency of the two modes increased by an average of 1.4 GHz while the resonance bandwidth, or mode splitting, increased by 0.3 GHz.

Figure 3(d) shows the cumulative sum of the amplitude of all resonance modes plotted as a function of H for each specimen. Clearly, the decrease in the absorption amplitude of each specimen is consistent with a decrease in the area of the ab plane. This trend is observed in both the FFM and CSL phases. The differences in the absorption amplitudes of the FFM and CSL phases reflect how the microwave field couples differentially to the helical spin configuration. Note that the amplitude of the resonance signal varies significantly near H_J and H_C. In the FFM phase, before H_J, there are small oscillations in the amplitude of the resonance modes followed by an abrupt decrease in the amplitude, at H_J, as the CSL phase is reached. In contrast, the transition from the CSL to the FFM phase, which is characterized by an asymptotic decrease in the resonance frequency, exhibits a

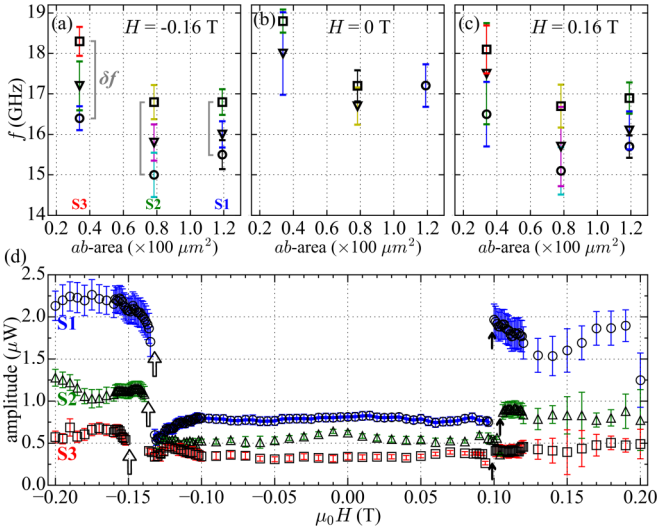

FIG. 3. (a)–(c) Plots of the resonance frequency (markers) and linewidths (vertical bars) at the indicated values of H, as a function of the area of the ab plane of S1, S2, and S3. (d) Cumulative sum of the absorption amplitude of all modes as a function of H of all specimens. Vertical bars correspond to the sum of the fitting error of each contributing resonance mode. The upward pointing line and thick arrows indicate the field position of H_J and H_C, respectively.

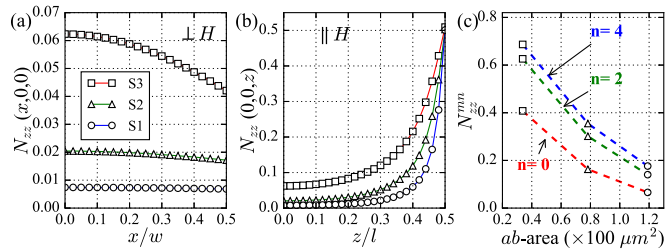

FIG. 4. (a)-(b) Plot of N_{zz} as a function of the normalized distance between the center and the edge of the rectangular element, along the directions x and z, respectively, calculated using Eq. (16) of Ref. [40]. The calculated $N_{zz}(0, y, 0)$ (not shown) was constant along the thickness. (c) Plot of the effective demagnetization factor N_{zz}^{mn} (calculated from Eq. (9) in Ref. [27]), for the values of n indicated by the dashed lines, as a function of the area of the ab plane.

gradual reduction in the amplitude of the dominant modes as H_C is approached. Immediately above H_C the amplitude of the resonance modes increases steadily, resembling the recovering of the ferromagnetic alignment from a magnetic state with zero net magnetic moment (softening). At fields well above H_C, the amplitude of the absorption in the fully formed FFM phase appears to be vary slightly around a constant value. The origin of the difference between the absorption amplitude of the FFM phase at positive (FFM1) and negative (FFM2) fields [also observed in Figs. 2(d), 2(f), and 2(h)] is still unclear, but it could mean that the FFM state before and after the helical phase is not exactly the same due to interface pinning or the strong demagnetization fields near the edges of the specimen. Alternatively, this effect could be related to amplitude nonreciprocity of the spin wave modes (nonzero wave number), whose excitation efficiency may differ when the polarity of H is changed. The nonreciprocity aspect of this magnetic system will be discussed elsewhere.

III. DISCUSSION: FFM

The FFM phase of the specimens investigated here may be described as in-plane magnetized rectangular elements of a ferromagnetic material with finite dimensions and saturated along its length by an external magnetic field. The exact solution for the magnetization dynamics in systems under spatial confinement along all directions cannot be easily obtained, as highlighted in Ref. [27]. This is particularly so for the present case, where an accurate solution would require the full account of the spin canting near the edges of the specimen, pinning conditions, inhomogeneous demagnetization fields, antisymmetric exchange interaction, and the exact nature of the symmetric exchange interaction, which is known to have different values along l (parallel to the ab plane) and w (perpendicular to the ab plane) due to the planar symmetry of the spin system [22,28]. In the case of nanometer-sized elements of soft ferromagnetic materials such as $Ni_{80}Fe_{20}$, one may resort to numerical simulations in order to accurately determine the precession modes. However, in the case of micrometer-sized elements presented here, such task is considered cumbersome due to both the nature of the magnetic system and limited computational resources. As such, a number of approximations must be taken into account in order to provide the simplest and yet sufficiently accurate analytical model capable of producing a good quantitative agreement with the experimental data.

With the above in mind, a parallel is drawn to a magnetic system consisting of rectangular elements of a soft ferromagnetic material with the same dimensions of S1, S2, and S3. This problem was previously discussed in the context of the dispersion relation of spin waves excited parallel or perpendicular to the in-plane magnetization [5,27,29–33], developed from a more general model for the description of the dipole-exchange spin wave spectrum with mixed boundary conditions [34–37]. The necessary approximations are now briefly outlined.

The resonance modes of an in-plane magnetized rectangular element are characterized by quantization conditions due to spatial confinement and nonuniform demagnetization fields, resulting in a set of allowed wave numbers k_x, k_y, and k_z. In order to obtain an approximate solution for the two in-plane dynamic magnetization components, it was considered that these could be treated independently [27,38,39]. Thus, the quantization of m_x is treated as a transversely magnetized stripe while the quantization of m_z is treated similarly to the case of a longitudinally magnetized stripe. The quantization condition of m_x is $k_{mx} = (m+1)\pi/w_{\text{eff}}$, with w_{eff} being an effective width of a given precessional mode [27,32] and m an integer number. This leads to solutions proportional to $\cos(k_{mx}x)$ and $\sin(k_{mx}x)$ for the symmetric and antisymmetric spatial distribution of the dynamic component m_x, respectively. Similarly, the quantization condition for m_z is $k_{nz} = (n+1)\pi/l_{\text{eff}}$ [27], with $n = 0, 1, 2, \ldots$.

Figure 4 shows the variation of the demagnetization factor N_{zz} [40] along the in-plane directions perpendicular (a) and

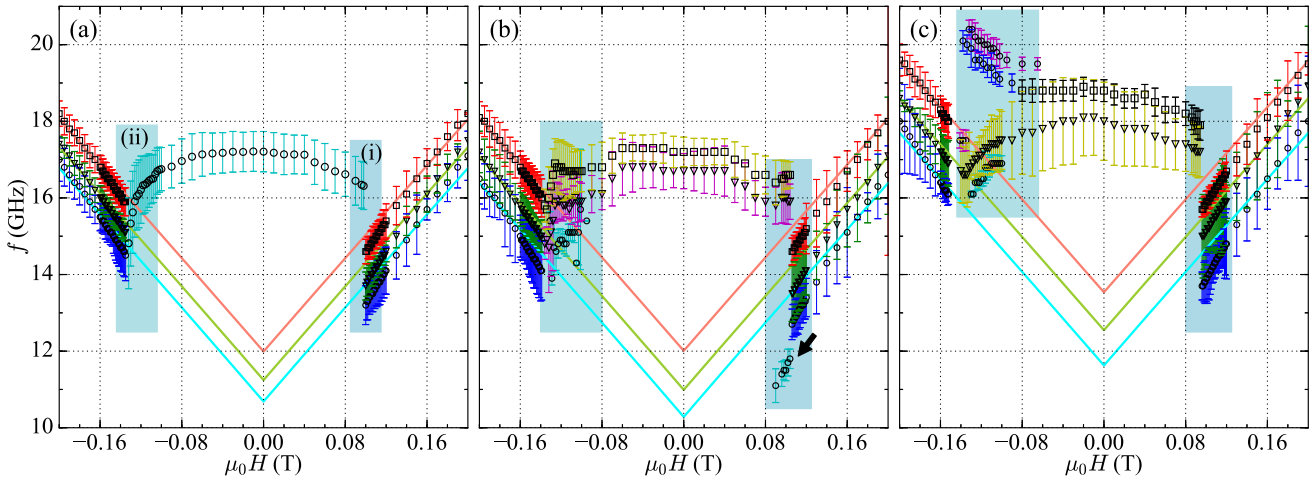

FIG. 5. (a)–(c) Resonance frequency (markers) and linewidths (vertical bars) of each mode plotted as a function of H for the specimens S1 to S3, respectively. The continuous lines correspond to a fit to Eq. (1). The colored rectangles (i) and (ii) indicate the field regions in the vicinity of H_J and H_C, respectively. The tilted arrow in (b) highlights the Kittel-like mode extending to the CSL phase.

parallel (b) to the direction of H, for all specimens. The smaller value of l, or, equivalently, the less rectangular shape of S3, resulted in larger and more nonuniform N_{zz}. Importantly, note that N_{zz} is only pronouncedly nonuniform along the direction of H (and l). This dependence will reflect on the resonance modes which are expected to be nonuniform along the length of the specimen. As a consequence of the varying demagnetization fields, the spatial distribution of the precession amplitude will not necessarily correspond to the physical dimensions w and l of the specimen. This justifies the use of effective geometrical parameters w_{eff} and l_{eff} within which the net internal field produces a valid solution for a given resonance mode.

Taking all the above into consideration, the approximate expression for the dipole-exchange spin waves modes in nonellipsoidal elements may be written in the form of the Herring-Kittel formula [27,34,36]

$$\omega_{mn} = \left[\omega_H^{mn} + \omega_M\left(\alpha_c k_{mx}^2 + \alpha_{ab} k_{nz}^2\right)\right]\left[\omega_H^{mn} + \omega_M\left(\alpha_c k_{mx}^2 + \alpha_{ab} k_{nz}^2\right) + \omega_M F_{mn}(k_{mn}t)\right], \quad (1)$$

where $\omega_M = \gamma M_s$, with γ being the gyromagnetic ratio (29.6 GHz/T) and $M_s = 0.22$ T the saturation magnetization [24]. The term $\omega_H^{mn} = \omega_H - \omega_M N_{zz}^{mn}$ corresponds to the net internal field acting on a given resonance mode (m, n). The effective demagnetization factor N_{zz}^{mn} is calculated following an integration of the dynamic magnetization and demagnetization field over the volume of the specimen, for each resonance mode (m, n) (Eq. (9) in Ref. [27]). The exchange constants α_c and α_{ab} are 4.2×10^{-12} and 3.36×10^{-11} Jm^{-1}, respectively [28]. The wave number sum is defined as $k_{mn}^2 = k_{mx}^2 + k_{nz}^2$. Experimentally, the largest excitation wave number $k^{\max} = 2\pi/S$ is limited by the width, S, of the signal line. In the present paper, the dimensions of the specimens are comparable to the width (S) of the signal line and are therefore comparable to the wavelength of the excitation field. In this limit, the terms associated with the exchange interaction may be maintained, despite their small contribution to the resonance frequency [41]. The term $F_{mn}(k_{mn}t)$ (shown in Appendix A) accounts for the dipole-dipole interaction term.

Figure 5 shows the resonance data overlaid with a fitting to Eq. (1) in the FFM phase ($|\mu_0 H| \geqslant 0.15$ T) of each resonance mode. It was assumed that the modes at higher, intermediate, and lower frequencies corresponded to having n as 0 and the even numbers 2 and 4, respectively, while keeping $m = 0$. The modes corresponding to $n = 2$ and 4 appeared to be more sensitive to the nonuniform demagnetization field along the direction parallel to H, which supports the choice of n (m_z) and not m (m_x). The fact that the demagnetization factor N_{zz}^{mn}, shown in Fig. 4(c), increases with increasing n appears to be supportive of the choice of $n = 2$ and 4.

The free parameters of the fit to Eq. (1), w_{eff} and l_{eff}, varied within the ranges [0.02–1] $\times$ w and [0.1–10] $\times$ l. The fact that w_{eff} and l_{eff} have the same order of magnitude of w and l suggests that the choice of $n = 2$ and $n = 4$ was reasonable. It should be stressed that the free parameters depended strongly on the assumed values of α_c, α_{ab} and the excitation wave number. Note that the fitting does not account for the existence of pinning at the interfaces, which would easily affect the absolute values of the free parameters w_{eff} and l_{eff}. In order to deepen the understanding about the spatial distribution of the modes, micromagnetic simulations and time and space-resolved magnetization dynamics experiments would be necessary.

Importantly, both the absolute value and the separation between N_{zz}^{00}, N_{zz}^{02}, and N_{zz}^{04} decrease with increasing area of the ab plane, which shows a qualitatively similar behavior to that of the frequency separation between the resonance modes of each specimen, as shown in Figs. 3(a)–3(c).

IV. DISCUSSION: CSL

Next, we discuss the resonance response of the CSL.

In the limit of bulk-size specimens, the density of the CSL (number of MKs) varies smoothly near 0 T and decreases asymptotically as the external field approaches H_C, resulting in a smoothly varying and almost symmetric field

dependence with regards to 0 T [13,15,21,22,42]. In sample S1, we observe only a single resonance mode across the entire CSL phase and, with the exception of the frequency jump at H_C, which is indicative of hysteresis, the resonance frequency varies rather smoothly near 0 T and decreases asymptotically near H_C. Provided this sample is the largest in our comparative study, it can said that S1 is the best available approximation to the response of a bulk-size specimen. If we neglect the hysteresis, the domelike field dependence observed in S1 is qualitatively consistent with the theoretical models discussed in Refs. [19,22,23,42]. However, because these models assume a one-dimensional spin structure with infinite length, there is a need to develop a more adequate scenario to quantitatively describe the spin dynamics in the helimagnetic phase. A theoretical description of the dynamics of the helimagnetic phase or the CSL phase in finite systems is a very nontrivial problem due to the interplay between the boundary spins and the demagnetization effects. Recent experimental studies on other compounds acknowledge that the helimagnetic phase is an open and difficult problem to tackle from the theoretical standpoint [2,8].

In the present paper, we present a model which is a step towards a more suitable approach compared to Refs. [19,22,23,42]. One in which the finite dimensions of the system, imposed via a pinning field at the boundaries of the spin system, contribute to the spin dynamics of the CSL. The outcome of the analysis of the model (see details in Appendix B) is that the collective resonance in the CSL results from standing waves. The spatial period of these waves is derived from the condition of matching the frequencies of the internal and edge spins oscillations. The dynamics of the latter is controlled by an additional field H_{edge} and the absence of one of the nearest neighbors. As a result, the resonance frequency on the CSL is given by

$$\omega_{\text{res}}^2 = \frac{\beta_x^2}{\kappa^4}\kappa'^2\,\text{sn}^2(\alpha_0,\kappa')\left[\kappa'^2\,\text{sn}^2(\alpha_0,\kappa') - 4\left(1-\frac{D}{J}\frac{\kappa}{\sqrt{\beta_x}}\right)\right], \tag{2}$$

where $\text{sn}(\cdots)$ is a Jacobi elliptic function, and κ and κ' are the elliptic modulus and complementary elliptic modulus, respectively; $\beta_x = H_x/JS$ is the external magnetic field. The real parameter α_0 is determined by the relation (B22) shown in Appendix B. The terms D and J account for the antisymmetric and symmetric exchange interaction terms, respectively. As illustrated in the Fig. 6, the resonance curve obtained with the help of Eq. (2) reproduces the domelike field dependence observed in the experimental data. Thus, a driving ac field applied parallel to the helical axis excites standing waves of even parity, whose period is incommensurate to the length of the sample due to the moving edge spins (see the animation in the Supplemental Material [43]). Naturally, these standing wave modes are expected to have higher order modes, whose field dependence has not yet been clearly identified in the numerical results.

The model mentioned above provides a satisfactory description of the resonance mode observed in S1, as well as it supporting the existence of multiple resonance modes which, experimentally, may correspond to the two modes observed in S2 and S3. However, this model does explain the reason why the mode splitting is so sensitive to the specimen size, especially considering that from S1 to S3 we only increase the area of the magnetization plane. This may be due to the fact that the spatial profile of the demagnetization fields is not taken in consideration.

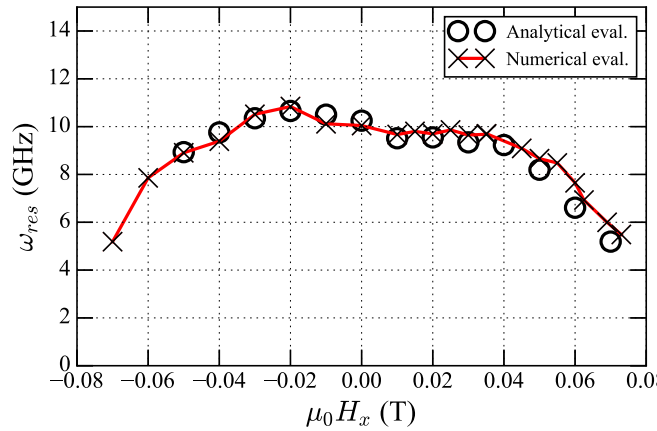

FIG. 6. Analytical and numerical evaluation (from Landau-Lifshitz equations) of the resonance of even parity of the CSL, based on Eq. (2), as a function of the external field. The parameters used in the calculations were $D/J = 0.16$, $J = 10$ K, and $H_{\text{edge}} = 0.1$ T, and the length of the spin chain was set to $L = 411$ (10 MKs).

The present experimental results, summarized in Fig. 3(a)–3(c), and the calculated mode splitting in the FFM phase, shown in Fig. 4(c) for n (0,2,4), suggest that changes in the spatial distribution of the demagnetization fields affected the frequency splitting between the modes, in both the CSL and the FFM phases. In Fig. 5 the vertical bars correspond to the half-width at half-maximum obtained from the Lorentzian fit to the experimental data. These help for visualizing changes in the frequency splitting with varying area of the ab plane. The emergence of two resonance modes and the increase in the frequency splitting between the resonance modes with decreasing length of the specimens can in part be attributed to changes in the demagnetization fields. On the other hand, because the frequency splitting of the resonance modes is maintained across the entire field range of the CSL, where the net moment is close to zero, the effect of the demagnetization fields is not straightforward and requires further evaluation.

There are two additional experimental features of relevance but for which there is no clear micromagnetic picture: the hysteresis effect observed in the decreasing field branch (near H_J) and the uncharacteristic resonance behavior near both H_J and H_C.

The hysteresis region—that is, the field region on the descending field branch where $|H_C| > H > H_J$—is almost the same on all specimens, and therefore is independent of the area of the ab plane. Recently, the hysteresis has been discussed in terms of a surface barrier energy, which provides an understanding of how MKs enter the finite-size specimen when sweeping the magnetic field from the FFM to the CSL phase [18,44]. In particular, Ref. [44] shows a good agreement between the calculated surface energy barrier and the magnetoresistance measurements where the ratio $H_J/H_C = 0.4$ is observed on all specimens. However, in the

present experiments we obtain a ratio H_J/H_C of ~ 0.7. Thus, the implications of the surface barrier on the magnetization dynamics experiments have yet to be clarified.

The uncharacteristic resonance behavior observed in the vicinity of both the H_J and H_C [regions (i) and (ii) in Fig. 5(a)] appears to be particularly sensitive to changes in the length of the ab plane. Take the following instances: In the field-decreasing branch of S2 we observe a Kittel-like mode coexisting with the CSL resonance, when H is just below H_J. This mode is indicated by the tilted arrow in Fig. 5(b). In the field-increasing branch of S2 there are hints of a third resonance mode in the vicinity of H_C, as illustrated by the red horizontal arrow in Fig. 2 (b). Interestingly, the increasing-field branch of S3 exhibits two additional resonance modes with a Kittel-like, linear slope, as indicated by the red arrows in Fig. 2(c). The coexistence of resonance modes with CSL and Kittel-like field dependence near H_J and H_C could be explained by the overlap of the CSL phase with the FFM phase. In a recent report on the skyrmion phase of a different compound [8], the coexistence of two magnetic phases was broadly attributed to softening of the magnetization. In the present paper we argue that the mixed phase or softening of the magnetic phases could be enabled by the inhomogeneous distribution of demagnetization fields near the edge of the specimens. Importantly, the CSL density varies rapidly near H_J, so we argue that the sudden vanishing of these Kittel-like modes is linked to a sharp decrease in the number of solitons. This highlights the importance of considering the competition between the nonuniform demagnetization fields and the field which drives the discrete changes in the number of MKs in the CSL phase, as such aneffect contributes to deviations from the asymptotic behavior of a single mode. Further investigations, in terms of both the static and the dynamic response, are necessary to clarify the mechanisms governing the phase transitions.

V. CONCLUSIONS

In this paper, we showed that altering dimensions of the specimen causes interesting modifications to the standing spin wave modes of the chiral spin soliton lattice. Thus, finite size effects, either via demagnetization field or boundary effects, play an important role in defining the frequency range and bandwidth of the magnetic resonance response. The resonance frequency and bandwidth were modified by several gigahertz, up to the point when mode splitting occurred on the CSL response of the smallest specimens. The results and the models presented here suggest that the inhomogeneity of the demagnetization fields contributes to the frequency splitting between the resonance modes. However, the nature of this effect is still under consideration, as the existing theoretical models cannot quantitatively reproduce the finite size of the CSL.

Importantly, it is observed that (at low fields) the resonance of the CSL maintains its overall field dependence, which indicates that the coupling between the microwave field components and the CSL texture is not prone to changes in the area of the magnetization plane. However, this may not hold valid if we consider the emergence of the field-dependent modes near H_C. Thereby, the shape appears to contribute indirectly to the polarization-dependent resonant absorption of the CSL. The focus should now be on changing the orientation of the crystal with regards to the microwave excitation field components. Further experimental work will open new avenues for exploring the microwave response in the phase transition for example via quantized microwave response or microwave switching of magnetoresistance states.

ACKNOWLEDGMENTS

The authors thank Y. Kato and B. Zingsem for insightful discussions, and K. Inoue and J. Akimitsu for promoting discussions around the topic of chiral magnetism. The authors acknowledge support from Grants-in-Aid for Scientific Research (No. 25220803, No. 17H02767, No. 17H02923, and No. 17F17316), Chirality Research Center (Crescent) of Hiroshima University, JSPS, RFBR under the Japan-Russia Research Cooperative Program, JSPS Core-to-Core Program "Advanced Research Networks" and support by the Ministry of Education and Science of the Russian Federation under Grant No. MK-1731.2018.2. A.S.O. and Vl.E.S. acknowledge funding by the RFBR, Grants No. 17-52-50013 and No. 18-32-00769 (mol_a), and by the Foundation for the Advancement of Theoretical Physics and Mathematics BASIS, Grant No. 17-11-107.

APPENDIX A: MAGNETOSTATIC MODES IN THICK RECTANGULAR ELEMENTS

The term $F_{mn}(k_{mn}t)$, used in Eq. (1), accounts for the dipole-dipole interaction and corresponds to [27,34,36]

$$F_{mn}(k_{mn}t) = 1 + P(k_{mn}t)[1 - P(k_{mn}t)] \times \left(\frac{\omega_M}{\omega_H^{mn} + \omega_M(\alpha_c k_{mx}^2 + \alpha_{ab}k_{nz}^2)}\right)\frac{k_{mx}^2}{k_{mn}^2} - P(k_{mn}t)\frac{k_{nz}^2}{k_{mn}^2}, \tag{A1}$$

where $P(k_{mn}L)$ corresponds to

$$P(k_{mn}t) = 1 - \frac{1 - \exp(-k_{mn}t)}{k_{mn}t}, \tag{A2}$$

APPENDIX B: RESONANT STANDING WAVES IN SOLITON LATTICE

The appearance of the domelike field dependence of the resonance profile for the soliton lattice may be explained in the model of resonance standing waves. To support this claim, the one-dimensional classical sine-Gordon model may be examined,

$$\mathcal{H} = \frac{JS^2}{2}(\partial_z\theta)^2 + \frac{JS^2}{2}\sin^2\theta(\partial_z\varphi)^2 + DS^2\sin^2\theta\partial_z\varphi - SH_x\sin\theta\cos\varphi, \tag{B1}$$

which describes classical spins $\mathbf{S} = S(\sin\theta\cos\varphi, \sin\theta\sin\varphi, \cos\theta)$ located inside the chain of the length $[-L/2, L/2]$.

The dynamical equations derived from the Hamiltonian describe evolution of the spin degrees of freedom,

$$\partial_\tau\theta = -\sin\theta\partial_z^2\varphi - 2\cos\theta\partial_z\theta\partial_z\varphi - 2\frac{D}{J}\cos\theta\partial_z\theta + \beta_x\sin\varphi, \tag{B2}$$

$$-\sin\theta\partial_\tau\varphi = \sin\theta\cos\theta(\partial_z\varphi)^2 - \partial_z^2\theta + 2\frac{D}{J}\sin\theta\cos\theta\partial_z\varphi - \beta_x\cos\theta\cos\varphi, \tag{B3}$$

where the dimensionless time $\tau = t\frac{JS}{\hbar}$ (for $J \sim 100$ K this corresponds to 10^{-13} s) and the magnetic field $\beta_x = H_x/JS$, where $\beta_x \sim 10^{-3}$ equivalent to 10^3 Oe, are introduced.

To parametrize a ground state of the system in the form of the simple spiral, the solution $\varphi_0(z) = qz$ with the unknown constant q is used. At nonzero external magnetic field, when the soliton lattice of finite length occurs, either the function $\varphi_0(z) = \pi - 2\mathrm{am}[\frac{\sqrt{\beta_x}}{\kappa}(z - z_0) + K]$ or $\varphi_0(z) = -2\mathrm{am}[\frac{\sqrt{\beta_x}}{\kappa}(z - z_0)]$ are taken, depending on the number of kinks confined in the soliton lattice, even or odd, respectively. Here, $\mathrm{am}(\cdots)$ is the Jacobi amplitude with the modulus κ; K is the elliptic integral of the first kind; z_0 is a center position.

The fluctuations above these nonuniform magnetic backgrounds can be formulated as

$$\varphi(z,\tau) = \varphi_0(z) + \chi(z)Z(\tau), \tag{B4}$$

$$\theta(z,\tau) = \frac{\pi}{2} + u_0(z)\xi(\tau), \tag{B5}$$

where separation of variables is realized through the time-dependent collective coordinates $Z(\tau)$ and $\xi(\tau)$ with the space-dependent amplitudes $\chi(z)$ and $u_0(z)$, respectively.

The solution of Eqs. (B2) and (B3) provides

$$Z(\tau) = \mathcal{A}\cos(\Omega\tau + \alpha), \tag{B6}$$

$$\xi(\tau) = -\frac{\mathcal{A}}{\mathcal{C}_2}\Omega\sin(\Omega\tau + \alpha), \tag{B7}$$

with the unknown amplitude $\mathcal{A}$ and the phase α. The frequency is expressed via some constants $\mathcal{C}_{1,2}$ that arise after separation of variables and appear in the equations for the spatial parts of the fluctuations:

$$-\partial_z^2\chi(z) + \beta_x\cos\varphi_0\,\chi(z) = \mathcal{C}_1 u_0(z), \tag{B8}$$

$$\partial_z^2 u_0 + (\partial_z\varphi_0)^2 u_0(z) + 2(D/J)u_0(z)\partial_z\varphi_0 - \beta_x u_0(z)\cos\varphi_0 = \mathcal{C}_2\chi(z). \tag{B9}$$

A treatment of dynamics of the boundary spins requires a separate analysis based on the Hamiltonian

$$\mathcal{H}_R = -J\mathbf{S}_{L/2-1}\cdot\mathbf{S}_{L/2} + D[\mathbf{S}_{L/2-1}\times\mathbf{S}_{L/2}]_z - (H_x + H_{\mathrm{edge}})S^x_{L/2} \tag{B10}$$

for the right edge spin and a similar counterpart for the left one with $z = -L/2$. In the model we assume that the additional pinning field H_{edge} affects significantly the boundary spins.

Minimization of the energy originated from the Hamiltonian (B10) for the simple spiral results in the condition for the parameter q

$$0 = \sin q + (D/J)\cos q \mp (\beta_x + \beta_{\mathrm{edge}})\sin\varphi_{\mp L/2}, \tag{B11}$$

where $\beta_{\mathrm{edge}} = H_{\mathrm{edge}}/JS$, that predicts the arrangement at the boundaries $\sin\varphi_{-L/2} = -\sin\varphi_{L/2}$.

Formulation of fluctuations in terms of the collective coordinates ensures

$$u_0(L/2)\frac{d\xi(\tau)}{d\tau} = Z(\tau)\Bigg\{\left[\frac{d\chi}{dz} - \frac{1}{2}\frac{d^2\chi}{dz^2}\right]_{z=L/2} - \frac{D}{J}\left(\frac{d\varphi_0}{dz}\right)\left(\frac{d\chi}{dz}\right)_{z=L/2} + (\beta_x + \beta_{\mathrm{edge}}) \times \cos\varphi_0(N)\chi(L/2)\Bigg\}, \tag{B12}$$

$$\chi(L/2)\frac{dZ(\tau)}{d\tau} = \xi(\tau)\Bigg\{-\frac{du_0}{dz}\bigg|_{z=L/2} + \frac{1}{2}\frac{d^2u_0}{dz^2}\bigg|_{z=L/2} + \frac{1}{2}u_0(L/2)\left(\frac{d\varphi_0}{dz}\right)^2\bigg|_{z=L/2} + \frac{D}{J}u_0(L/2)\left[\frac{d\varphi_0}{dz} - \frac{1}{2}\frac{d^2\varphi_0}{dz^2}\right]_{z=L/2} - (\beta_x + \beta_{\mathrm{edge}})u_0(L/2)\cos\varphi_0(L/2)\Bigg\}, \tag{B13}$$

and similar equations for the left edge of the chain may be obtained. Since the solutions can be categorized by parity Eqs. (B12) and (B13) are sufficient only.

The dispersion law for standing waves for *the simple spiral* ($\beta_x = 0$) may be derived from Eqs. (B8) and (B9) in the form $k = k(\Omega)$:

$$k^2 = \tfrac{1}{2}\{q^2 + 2q(D/J)\} + \tfrac{1}{2}[\{q^2 + 2q(D/J)\}^2 + 4\Omega^2]^{1/2}. \tag{B14}$$

The standing waves of even parity are parametrized as

$$\chi^{(g)}(z) = \mathcal{C}_g\cos(kz), \qquad u_0^{(g)}(z) = \frac{\mathcal{C}_g}{\mathcal{C}_1}k^2\cos(kz), \tag{B15}$$

where $\mathcal{C}_g$ is an arbitrary constant and k, Ω are the wave vector and the eigenfrequency of the standing wave, respectively.

Using the functions (B15) one may find frequency of even-parity oscillations of the boundary spins from Eqs. (B12) and (B13):

$$\Omega_g^2 = \{k\tan(kL/2)(1 - (D/J)q) - k^2/2 - \beta_{\mathrm{edge}}\cos\varphi_0(L/2)\} \times\{k\tan(kL/2) - k^2/2 + q^2/2 + (D/J)q - \beta_{\mathrm{edge}}\cos\varphi_0(L/2)\}. \tag{B16}$$

A requirement of consistency of dynamics of the boundary and inner spins means that this relationship should be resolved together with Eqs. (B11) and (B14).

A similar consideration of the odd modes gives the result

$$\Omega_u^2 = \{k\cot(kL/2)(1-(D/J)q) + k^2/2 + \beta_{\rm edge}\cos\varphi_0(L/2)\} \times\{k\cot(kL/2) + k^2/2 - q^2/2 + (D/J)q + \beta_{\rm edge}\cos\varphi_0(L/2)\}. \quad \text{(B17)}$$

To illustrate, the data $\varphi_{L/2} = -63.053842$ and $q = -0.154326$ for the chain of the length $L = 411$ with $D/J = 0.16$ yield two lowest resonance frequencies for the even modes, $\Omega_g^{(1)} = 0.00098$ and $\Omega_g^{(2)} = 0.001067$, and for the odd modes, $\Omega_u^{(1)} = 0.00200$ and $\Omega_u^{(2)} = 0.002154$. Note that in the dimensionless units $\Omega = 10^{-4}$ corresponds to 1 GHz.

For *the soliton lattice* the system (B8)-(B9) for the inner spins is substituted for

$$\hat{L}_\varphi\chi(\bar{z}) = -\frac{\kappa^2}{\beta_x}\mathcal{C}_1 u_0(\bar{z}), \qquad \hat{L}_\theta u_0(\bar{z}) = \frac{\kappa^2}{\beta_x}\mathcal{C}_2\chi(\bar{z}) \quad \text{(B18)}$$

with the differential operators of the Lamé equation [19]

$$\hat{L}_\varphi = \frac{d^2}{d\bar{z}^2} - 2\kappa^2\mathrm{sn}^2(\bar{z}) + \kappa^2,$$
$$\hat{L}_\theta = \frac{d^2}{d\bar{z}^2} - 2\kappa^2\mathrm{sn}^2(\bar{z}) + \left(4 + \kappa^2 - 4\frac{D}{J}\frac{\kappa}{\sqrt{\beta_x}}\right), \quad \text{(B19)}$$

with the eigenfunctions $\nu_q(\bar{z})$ depending on the dimensionless coordinate $\bar{z} = \sqrt{\beta_x}(z - z_0)/\kappa$.

Making expansions of the fluctuations over the eigenfunctions one find the dispersion law in the parametric form

$$\kappa'^2\mathrm{sn}^2(\alpha,\kappa')\left[\kappa'^2\mathrm{sn}^2(\alpha,\kappa') - 4\left(1 - \frac{D}{J}\frac{\kappa}{\sqrt{\beta_x}}\right)\right] = \frac{\kappa^4}{\beta_x^2}\Omega^2, \quad \text{(B20)}$$

$$q_c = \frac{\sqrt{\beta_x}}{\kappa}\left[Z(\alpha,\kappa') + \frac{\pi\alpha}{2KK'}\right], \quad \text{(B21)}$$

which relates the momentum q_c with the frequency Ω via the real parameter $-K' < \alpha < K'$. Here, $Z(\alpha,\kappa')$ is the Jacobi zeta function, and K' denotes the complete elliptic integral of the first kind with complementary elliptic modulus $\kappa' = \sqrt{1-\kappa^2}$. This relationship is a counterpart of Eq. (B14) for the soliton lattice.

To achieve an agreement with dynamics of the boundary spins, the frequency should coincide with the similar expression derived from equations of motion for the boundary spins, as has been done for the simple spiral, Eq. (B16):

$$\Omega_{\rm SL}^2 = \frac{1}{\nu_{q_c}^2(\bar{z}_{L/2})}\left[\frac{\sqrt{\beta_x}}{\kappa}\nu'_{q_c}(\bar{z}_{L/2}) - \frac{1}{2}\frac{\beta_x}{\kappa^2}\nu''_{q_c}(\bar{z}_{L/2}) + 2\frac{D}{J}\frac{\beta_x}{\kappa^2}dn(\bar{z}_{L/2})\nu'_{q_c}(\bar{z}_{L/2}) + (\beta_x + \beta_{\rm edge})\cos\varphi_0(L/2)\nu_{q_c}(\bar{z}_{L/2})\right] \times\left[\frac{\sqrt{\beta_x}}{\kappa}\nu'_{q_c}(\bar{z}_{L/2}) - \frac{1}{2}\frac{\beta_x}{\kappa^2}\nu''_{q_c}(\bar{z}_{L/2}) - 2\frac{\beta_x}{\kappa^2}dn^2(\bar{z}_{L/2})\nu_{q_c}(\bar{z}_{L/2}) + \frac{D}{J}\left\{2\frac{\sqrt{\beta_x}}{\kappa}dn(\bar{z}_{L/2}) + \frac{1}{2}\beta_x\sin\varphi_0(L/2)\right\}\nu_{q_c}(\bar{z}_{L/2}) + (\beta_x + \beta_{\rm edge})\cos\varphi_0(L/2)\nu_{q_c}(\bar{z}_{L/2})\right]. \quad \text{(B22)}$$

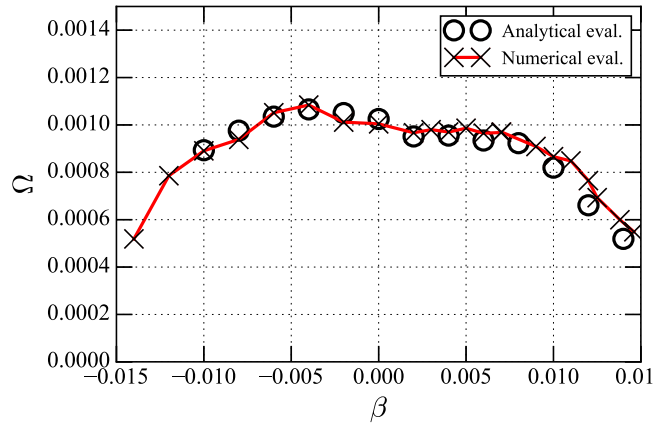

FIG. 7. Resonance frequencies for the lowest modes of even parity as a function of the external magnetic field β. The circles and triangles are results of analytical treatment, the crosses are found from numerical calculations of beatings. In dimensionless units $\Omega = 10^{-4}$ equals to 1 GHz and the field can be converter to units of $\mu_0 H$ (T) by multiplying β_x by a factor of 5.

The terms ν'_{q_c} and ν''_{q_c} correspond to $\frac{d\nu_{q_c}}{d\bar{z}}$ and $\frac{d^2\nu_{q_c}}{d\bar{z}^2}$. The result is valid for the even-parity standing waves with the eigenfunctions of the Lamé operators [19]

$$\nu_{q_c}(\bar{z}) = \frac{1}{\theta_4\left(\frac{\pi\bar{z}}{2K}\right)}\left[\theta_4\left(\frac{\pi}{2K}[\bar{z} - i\alpha - K]\right)e^{-i\bar{q}_c\bar{z}} + \theta_4\left(\frac{\pi}{2K}[\bar{z} + i\alpha - K]\right)e^{i\bar{q}_c\bar{z}}\right], \quad \text{(B23)}$$

where $\theta_{n=4}(z,q)$ is the Jacobi theta function with nome $q = \exp\frac{-\pi K'}{K}$. An analogous outcome may be obtained for odd modes in a straightforward manner.

Numerical assessment for the soliton lattice of $L = 411$ sites with $D/J = 0.16$, $\beta_{\rm edge} = 0.02$, and $\beta_x = 0.004$, which corresponds to $\kappa = 0.685\,283$, gives for the trial wave function $\varphi_0(z) = \pi - 2\mathrm{am}[\frac{\sqrt{\beta_x}}{\kappa}(z - z_0)]$, with the center position

$$z_0 = \frac{L}{2} - \frac{\kappa}{\sqrt{\beta_x}}K = 185.181$$

and the dimensionless coordinate of the right boundary site

$$\bar{z}_{L/2} = \frac{\sqrt{\beta_x}}{\kappa}\left(\frac{L}{2} + \frac{\kappa}{\sqrt{\beta_x}}K\right) = 20.7488.$$

The corresponding angle value equals to $\varphi_0(\bar{z}_{L/2}) = -32.3582$. Making use of Eqs. (B20), (B21), and (B22) we find eventually for the lowest even-parity modes $\Omega_g^{(1)} = 0.0009399$ and $\Omega_g^{(2)} = 0.0009706$.

As can be seen from Fig. 7, an appearance of the domelike field profile follows from the above analysis and numerical simulations of resonance via beating, as has been described in Ref. [23].

[1] M. Menzel, Y. Mokrousov, R. Wieser, J. E. Bickel, E. Vedmedenko, S. Blügel, S. Heinze, K. von Bergmann, A. Kubetzka, and R. Wiesendanger, Phys. Rev. Lett. **108**, 197204 (2012).

[2] T. Schwarze, J. Waizner, M. Garst, A. Bauer, I. Stasinopoulos, H. Berger, C. Pfleiderer, and D. Grundler, Nat. Mater. **14**, 478 (2015).

[3] Y. Togawa, Y. Kousaka, K. Inoue, and J.-I. Kishine, J. Phys. Soc. Jpn. **85**, 112001 (2016).

[4] M. Garst, J. Waizner, and D. Grundler, J. Phys. D **50**, 293002 (2017).

[5] A. V. Chumak, A. A. Serga, and B. Hillebrands, J. Phys. D: Appl. Phys. **50**, 244001 (2017).

[6] A. V. Chumak and H. Schultheiss, J. Phys. D **50**, 300201 (2017).

[7] T.-H. Kim, S. Cheon, and H. W. Yeom, Nat. Phys. **13**, 444 (2017).

[8] M. Weiler, A. Aqeel, M. Mostovoy, A. Leonov, S. Geprägs, R. Gross, H. Huebl, T. T. M. Palstra, and S. T. B. Goennenwein, Phys. Rev. Lett. **119**, 237204 (2017).

[9] I. Dzyaloshinsky, J. Phys. Chem. Solids **4**, 241 (1958).

[10] T. Moriya, Phys. Rev. **120**, 91 (1960).

[11] I. E. Dzyaloshinskii, Zh. Eksp. Teor. Fiz. **46**, 1420 (1964) [Sov. Phys. JETP **19**, 960 (1964)].

[12] T. Moriya and T. Miyadai, Solid State Commun. **42**, 209 (1982).

[13] Y. Togawa, T. Koyama, K. Takayanagi, S. Mori, Y. Kousaka, J. Akimitsu, S. Nishihara, K. Inoue, A. S. Ovchinnikov, and J. Kishine, Phys. Rev. Lett. **108**, 107202 (2012).

[14] Y. Togawa, T. Koyama, Y. Nishimori, Y. Matsumoto, S. McVitie, D. McGrouther, R. L. Stamps, Y. Kousaka, J. Akimitsu, S. Nishihara, K. Inoue, I. G. Bostrem, V. E. Sinitsyn, A. S. Ovchinnikov, and J. Kishine, Phys. Rev. B **92**, 220412 (2015).

[15] K. Tsuruta, M. Mito, Y. Kousaka, J. Akimitsu, J.-i. Kishine, Y. Togawa, H. Ohsumi, and K. Inoue, J. Phys. Soc. Jpn. **85**, 013707 (2016).

[16] F. J. T. Goncalves, T. Sogo, Y. Shimamoto, Y. Kousaka, J. Akimitsu, S. Nishihara, K. Inoue, D. Yoshizawa, M. Hagiwara, M. Mito, R. L. Stamps, I. G. Bostrem, V. E. Sinitsyn, A. S. Ovchinnikov, J. Kishine, and Y. Togawa, Phys. Rev. B **95**, 104415 (2017).

[17] I. Stasinopoulos, S. Weichselbaumer, A. Bauer, J. Waizner, H. Berger, M. Garst, C. Pfleiderer, and D. Grundler, Sci. Rep. **7**, 7037 (2017).

[18] M. Mito, H. Ohsumi, K. Tsuruta, Y. Kotani, T. Nakamura, Y. Togawa, M. Shinozaki, Y. Kato, J.-i. Kishine, J.-i. Ohe, Y. Kousaka, J. Akimitsu, and K. Inoue, Phys. Rev. B **97**, 024408 (2018).

[19] J.-i. Kishine and A. Ovchinnikov, in *Solid State Physics* 1st ed. (Elsevier, New York, 2015), pp. 1–130.

[20] J.-i. Kishine, I. G. Bostrem, A. S. Ovchinnikov, and Vl. E. Sinitsyn, Phys. Rev. B **89**, 014419 (2014).

[21] K. Tsuruta, M. Mito, Y. Kousaka, J. Akimitsu, J. Kishine, Y. Togawa, and K. Inoue, J. Appl. Phys. **120**, 143901 (2016).

[22] J.-i. Kishine and A. S. Ovchinnikov, Phys. Rev. B **79**, 220405(R) (2009).

[23] J.-i. Kishine, I. Proskurin, I. G. Bostrem, A. S. Ovchinnikov, and V. E. Sinitsyn, Phys. Rev. B **93**, 054403 (2016).

[24] T. Miyadai, K. Kikuchi, H. Kondo, S. Sakka, M. Arai, and Y. Ishikawa, J. Phys. Soc. Jpn. **52**, 1394 (1983).

[25] Y. Kousaka, Y. Nakao, J. Kishine, M. Akita, K. Inoue, and J. Akimitsu, Nucl. Instrum. Methods Phys. Res., Sect. A **600**, 250 (2009).

[26] K. Tsuruta, M. Mito, H. Deguchi, J. Kishine, Y. Kousaka, J. Akimitsu, and K. Inoue, Phys. Rev. B **93**, 104402 (2016).

[27] K. Y. Guslienko, R. W. Chantrell, and A. N. Slavin, Phys. Rev. B **68**, 024422 (2003).

[28] M. Shinozaki, S. Hoshino, Y. Masaki, J.-i. Kishine, and Y. Kato, J. Phys. Soc. Jpn. **85**, 074710 (2016).

[29] J. Jorzick, S. O. Demokritov, C. Mathieu, B. Hillebrands, B. Bartenlian, C. Chappert, F. Rousseaux, and A. N. Slavin, Phys. Rev. B **60**, 15194 (1999).

[30] K. Y. Guslienko and A. N. Slavin, J. Magn. Magn. Mater. **215**, 576 (2000).

[31] M. Bailleul, D. Olligs, C. Fermon, and S. O. Demokritov, Europhys. Lett. **56**, 741 (2001).

[32] K. Y. Guslienko, S. O. Demokritov, B. Hillebrands, and A. N. Slavin, Phys. Rev. B **66**, 132402 (2002).

[33] K. Y. Guslienko and A. N. Slavin, J. Magn. Magn. Mater. **323**, 2418 (2011).

[34] C. Herring and C. Kittel, Phys. Rev. **81**, 869 (1951).

[35] T. W. O'Keeffe and R. W. Patterson, J. Appl. Phys. **49**, 4886 (1978).

[36] B. A. Kalinikos and A. N. Slavin, J. Phys. C **19**, 7013 (1986).

[37] B. A. Kalinikos, M. P. Kostylev, N. V. Kozhus, and A. N. Slavin, J. Phys.: Condens. Matter **2**, 9861 (1990).

[38] C. Bayer, J. Jorzick, B. Hillebrands, S. O. Demokritov, R. Kouba, R. Bozinoski, A. N. Slavin, K. Y. Guslienko, D. V. Berkov, N. L. Gorn, and M. P. Kostylev, Phys. Rev. B **72**, 064427 (2005).

[39] C. Bayer, J. Jorzick, S. O. Demokritov, A. N. Slavin, K. Y. Guslienko, D. V. Berkov, N. L. Gorn, M. P. Kostylev, and B. Hillebrands, in *Spin Dynamics in Confined Magnetic Structures III*, Topics in Applied Physics Vol. 101 (Springer, Berlin, 2006), pp. 57–103.

[40] R. I. Joseph and E. Schlömann, J. Appl. Phys. **36**, 1579 (1965).

[41] A. G. Gurevich and G. A. Melkov, in *Magnetization Oscillations and Waves* (CRC, New York, 1996).

[42] V. V. Kiselev and A. A. Raskovalov, J. Exp. Theor. Phys. **116**, 272 (2013).

[43] See Supplemental Material at http://link.aps.org/supplemental/10.1103/PhysRevB.98.144407 for animation showing the profile of standing waves of even parity, whose period is incommensurate to the length of the sample due to the moving edge spins.

[44] M. Shinozaki, Y. Masaki, R. Aoki, Y. Togawa, and Y. Kato, Phys. Rev. B **97**, 214413 (2018).